

Nanoscale Control of Molecular Self-assembly Induced by Plasmonic Hot-Electron Dynamics

Sabrina Simoncelli^{1‡*}, Yi Li^{1‡}, Emiliano Cortés¹ and Stefan A. Maier^{1,2}

¹*The Blackett Laboratory, Department of Physics, Imperial College London, London SW7 2AZ, United Kingdom*

²*Chair in Hybrid Nanosystems, Faculty of Physics, Ludwig-Maximilians-Universität München, 80799 München, Germany.*

[‡]*These authors contributed equally to this work*

** Email: s.simoncelli@imperial.ac.uk*

Contents

Materials and Methods

S1. Surface coverage and electrochemical measurements

S2. Dual-hyperbolic two-temperature model

S3. Sorting and purification of colloidal nanoparticles

Table S1. Metallic DNA-PAINT docking and imager sequences

Supporting Figures

Fig. S1. Surface coverage estimation from electrochemical measurements.

Fig. S2. Super resolution m-PAINT imaging of gold nanostructures.

Fig. S3. Localization precision and cross-sectional histograms.

Fig. S4. Plasmonic response of gold nanotrimer structures.

Fig. S5. Super-resolution m-PAINT imaging of thiol-desorption and ligand replacement from individual gold nanotrimer structures.

Fig. S6. Controlling thiol-desorption and ligand replacement from gold nanotrimer structures with polarized light illumination.

Fig. S7. Plasmonic response of six-leg gold nanostructures.

Fig. S8. Plasmonic response of ‘ICL’ gold nanostructures.

Fig. S9. Plasmonic response of ‘L’ gold nanostructures.

Fig. S10. Numerical calculation of temperature profiles of plasmon-selective Au-S desorption on gold nanotrimers.

Fig. S11. Solution-based sorting of metal nanoparticles.

Supporting References

Materials and Methods

S1. Surface coverage and electrochemical measurements

In order to estimate the surface coverage of the mix monolayer (MCH + thiolated-DNA docking strand) we performed reductive electrodesorption measurements on polycrystalline preferred oriented Au (111) electrodes. Self-assembly conditions were identical to the ones described in the gold-sulfur functionalization section. Measurements were performed in a CHI600E Potentiostat, IJ Cambria Scientific Ltd. Electrodesorption curves were recorded in a three-electrode glass cell equipped with a Pt foil as counter electrode and an Ag/AgCl reference electrode. The amount of thiolate species on the Au substrates was measured by reductive desorption in 0.1 M NaOH by a potential scan run from -0.1 to -1.4 V at $v = 0.1 \text{ V s}^{-1}$. The electrochemically-active surface area of the Au electrodes was voltammetrically estimated in the same electrolyte (0.1 M NaOH solution) by recording a triangular potential sweep from -1.40 to 0.60 V at $v = 0.1 \text{ V s}^{-1}$ and considering that the charge density related to the electroreduction of a gold oxide monolayer is 0.44 mC cm^{-2} . Typical reductive desorption curves for the mix SAMs from the Au substrates are shown in Supplementary Figure S1. The cathodic peak correspond to the reductive desorption of the thiolate species from the Au surface. The charge density involved in these peaks gives an accurate estimation of the amount of chemisorbed thiolate to the Au surface. Integration of the voltammetric peaks show a value of $q \approx 80 \pm 5 \text{ } \mu\text{C cm}^{-2}$, that corresponds to a thiolate coverage $\theta \approx 1/3$, assuming one electron transfer for the reductive desorption reaction. The value $\theta = 1/3$ is the maximum surface coverage reached by thiolate species on Au surfaces.¹ From SEM images we estimated the surface area of a single leg ($A \approx 2.28 \times 10^4 \text{ nm}^2$) in the nanotrimer antenna design. Using the obtained value for the surface coverage on the Au (111) electrode, we estimate the number of Au-S bonds per leg of the nanotrimer antenna design to be 1.05×10^5 molecules in the mix monolayer. From these value and using reported data² on the coverage of thiolated ss-DNA under similar experimental conditions, we determined a ratio of $\sim 160/1$ of MCH/ss-DNA molecules in our mix monolayer.

S2. Dual-hyperbolic two-temperature model

Hot electrons excited upon resonant surface plasmons decay collide with electrons around the Fermi level. These hot electrons are then diffused into deeper parts of the electron gas at a speed ($< 10^4 \text{ m/s}$) much lower than that of the ballistic motion (close to the Fermi velocity $\sim 10^6 \text{ m/s}$) while transferring their energy to the lattice through electron-phonon coupling.³ The non-equilibrium between electrons and lattice has been observed experimentally^{4,5} and can be described by a well-established two-temperature model, which was originally proposed by Anisimov *et al.*⁶

We simulate the temporal dependence of the lattice temperature of gold nanostructures supported on a silica substrate and embedded in water by using the hyperbolic model to calculate the heat conduction, in both, electrons and phonons after femtosecond irradiation. The energy equation for the lattice becomes,

$$C_e \frac{\partial T_e}{\partial t} + C_e \tau_e \frac{\partial^2 T_e}{\partial t^2} = \kappa_e \nabla^2 T_e - G(T_e - T_l) - \tau_e \frac{\partial}{\partial t} G(T_e - T_l) + Q + \tau_e \frac{\partial Q}{\partial t}$$
$$C_l \frac{\partial T_l}{\partial t} + C_l \tau_l \frac{\partial^2 T_l}{\partial t^2} = \kappa_l \nabla^2 T_l + G(T_e - T_l) + \tau_l \frac{\partial}{\partial t} G(T_e - T_l)$$

where T_e and T_l are the electron and lattice temperature, τ_e and τ_l are the electron and lattice collision time of 0.04 ps and 0.8 ps for gold,⁷ respectively; κ_e and κ_l are the electronic and lattice thermal conductivity of gold; C_e and C_l are the electronic and lattice heat capacity and where $\kappa_e = \frac{T_e}{T_l} \kappa_{e,0}$ and $\kappa_{e,0} \approx \kappa_l$. Within the free electron gas model^{8,9} $C_e = \frac{\pi^2 k_B^2 n_e}{2E_F} T_e$ and can be associated to the free electron number density n_e . We use a gold-water extraction potential E_F of 3.72 eV.¹⁰ Since the Debye temperature for gold is 178 K at room temperature,¹¹ the electron-phonon coupling G for gold can be assumed to be independent to the electron temperature as 2.6×10^{16} W/(m³ K). Q represents the resistive loss of gold nanoantenna from optical absorption. The surface roughness as well as morphology induced effects has not been taken into account in our simulation.

S3. Sorting and purification of colloidal nanoparticles

Figure S11, shows a proof of concept that further explores the wavelength dependence of the Au-S bond cleavage in colloidal plasmonic antennas. Selective thiol displacement from a colloidal mix of 50 nm Au spherical nanoparticles (AuNPs) and 150×50 nm Au nanorods (AuNRs) was achieved by illuminating the solution at the resonance wavelength of one of the constituents (*i.e.* 780 nm, AuNRs longitudinal plasmon resonance) at a laser power below the onset energy for melting and reshaping of single gold nanorods.¹² Both types of nanoparticles were initially coated with a self-assembly monolayer of 4-mercaptobenzoic acid (MBA). After the illumination a clear aggregation of the AuNRs takes place as a consequence of thiol displacement only for this type of particles, as shown in the extinction spectra and SEM images for the pre/post irradiated solutions. AuNPs remain unaltered, highlighting the highly wavelength-dependent specificity of the process.

Description	Sequence
Docking P ₁	ThiolC6-SpacerC18-ATTACTTCTTT
Docking P ₂	ThiolC6-SpacerC18-ATGAGTTAATT
Imager P ₁ *	Atto655-AGAAGTAATG-3'
Imager P ₂ *	Atto655-TTAACTCATG-3'

Table S1. Metallic DNA-PAINT docking and imager sequences.

Supporting Figures

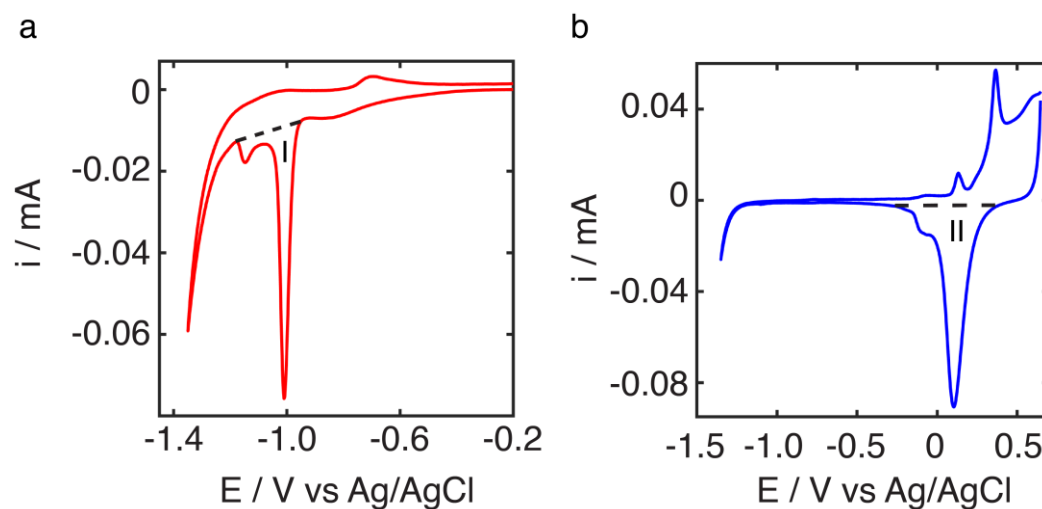


Figure S1. Surface coverage estimation from electrochemical measurements. **a**, Reductive electrodesorption curve for the mix monolayer (MCH + ss-DNA) SAM on a Au (111) substrate. Integration of the charge in peak I indicates the amount of Au-S bonds cleaved. **b**, Electrochemically active surface area of the Au electrode was determined after thiols desorption. Integration of the charge from peak II allows to estimate the charge density and surface coverage, as explained in S1.

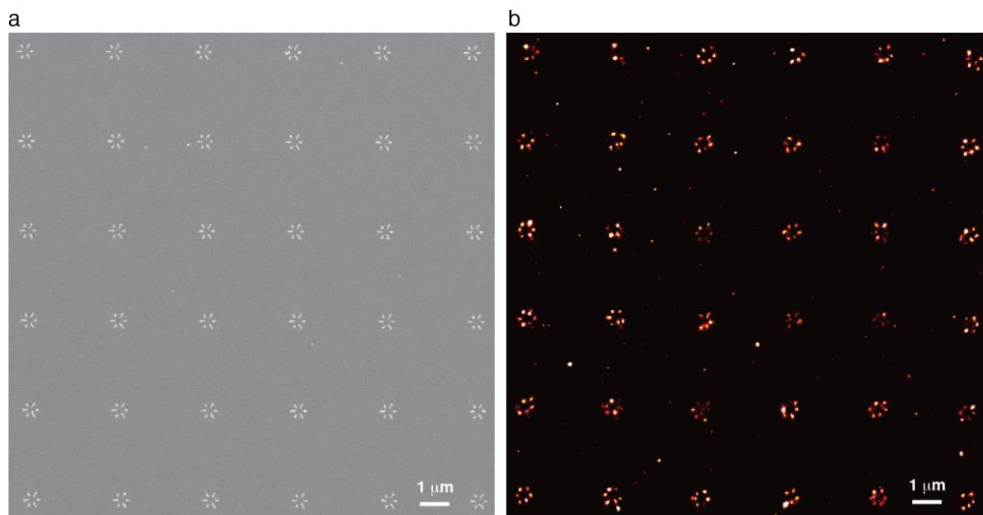


Figure S2. Super resolution m-PAINt imaging of gold nanostructures. **a**, SEM and **b**, super-resolved metallic DNA-PAINt image of a 6×6 array of individual six-leg nano-sized gold structures fabricated with electron beam lithography. m-PAINt movie was collected using 0.1 nM concentration of imager strand P₁* in imaging buffer C. The mean number of localizations per individual nanostructure is $1,458 \pm 332$.

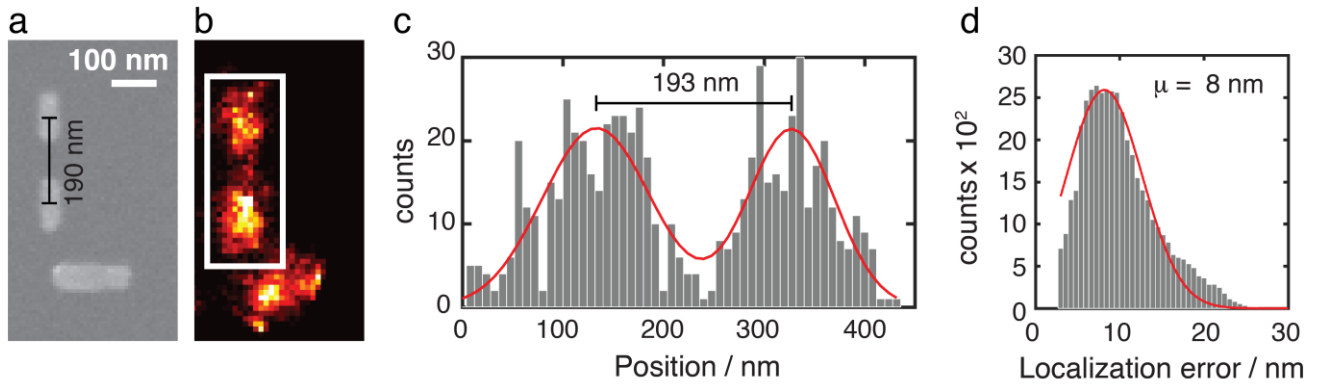


Figure S3. Localization precision and cross-sectional histograms. **a**, SEM and **b**, average super-resolved metallic DNA-PAINT image of 35 individual Au nanostructures functionalized with docking strand P₁ and composed of two sizes of nanorods with dimensions of 110×45 nm² and 180×40 nm². **c**, Cross-sectional histogram along the center line of the boxed area in **b** revealing a distance of ~193 nm as designed. **d**, Histogram of the error in the localization of single molecule events.

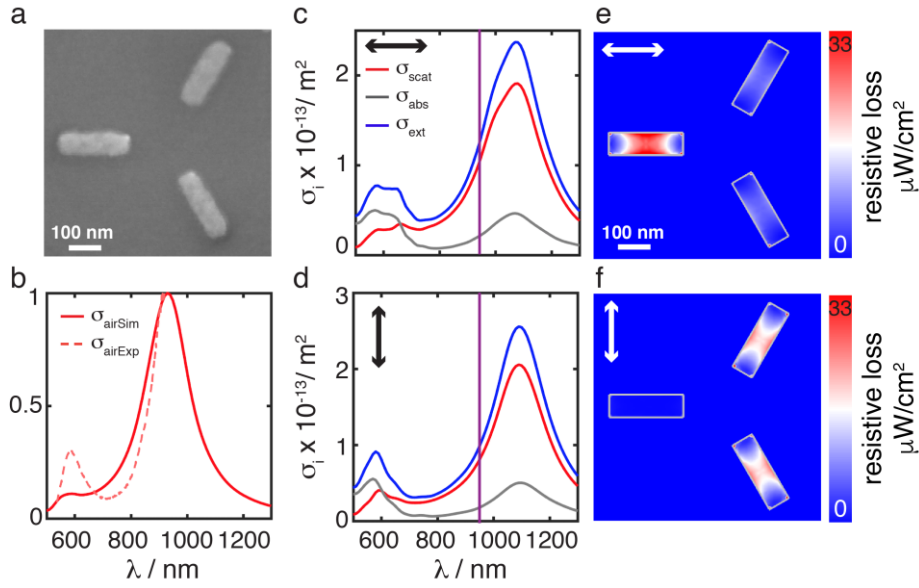


Figure S4. Plasmonic response of gold nanotrimer structures. **a**, SEM image of a gold trimer nano-sized structure composed of three identical nanorods with dimension of $180 \times 55 \text{ nm}^2$. **b**, FDTD-simulated (full line) and measured (dashed line) single-antenna scattering spectra in air. **c**, **d**, Simulated scattering (red), absorption (grey) and extinction (blue) spectra in water for parallel and perpendicular polarized illumination, respectively. Violet lines highlight the laser wavelength used in the desorption experiments (950 nm). **e**, **f**, Comsol simulations of the resistive loss distribution at 950 nm after femtosecond laser irradiation in water (fluence of 1.7 mJ/cm^2) for parallel and perpendicular incident polarization, respectively. Color scale bars represent the resistive losses values in $\mu\text{W}/\text{nm}^3$.

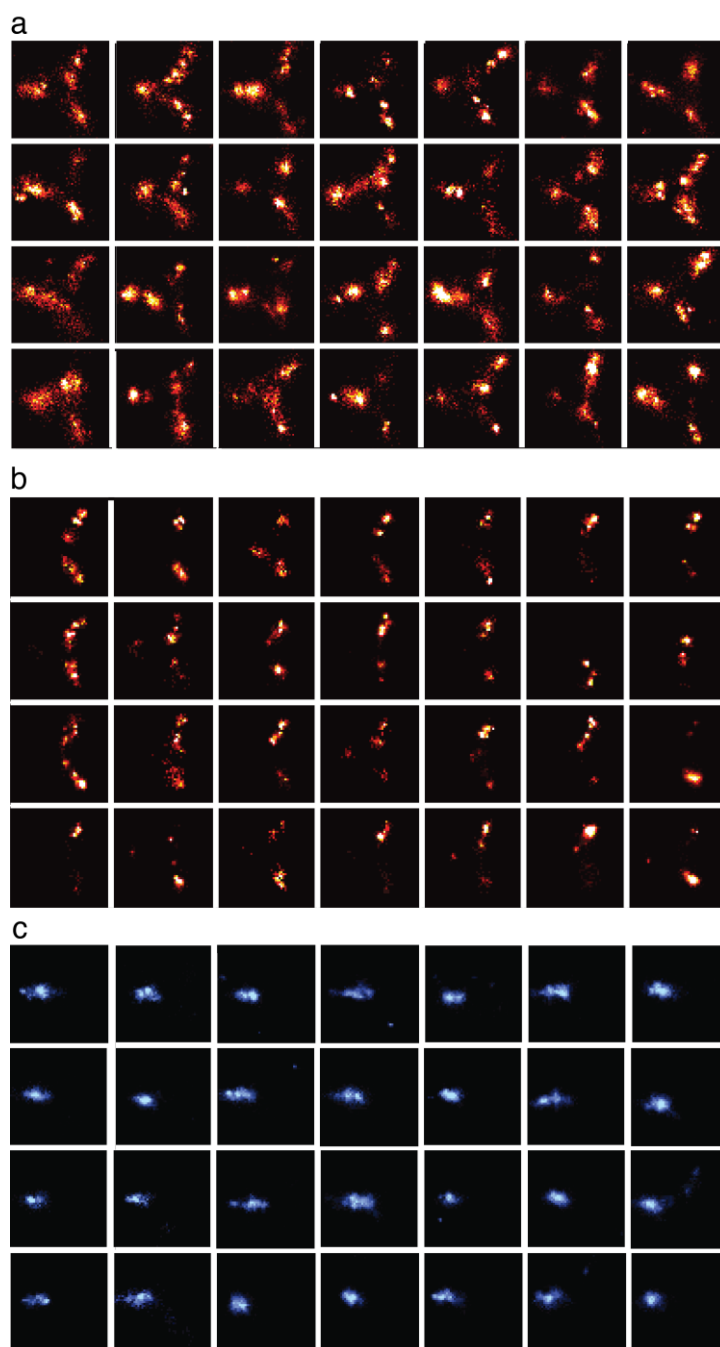


Figure S5. Super-resolution m-PAINt imaging of thiol-desorption and ligand replacement from individual gold nanotrimer structures. Cropped super-resolved metallic DNA-PAINt images of individual gold trimer nano-sized structures used to generate the high-density super-resolved images (see Figure 1c) before (**a**) and after (**b**, **c**) femtosecond laser irradiation (950 nm, 1.7 mJ/cm²) and re-functionalization (**c**) with the thiol-reactive docking strand P₂. The polarization of the light was aligned parallel to the horizontal leg of the trimer antenna. m-PAINt movie was collected using 1 nM or 2 nM concentration of imager strand P₁* (**a**, **b**) or P₂* (**c**) in imaging buffer C, respectively. Pseudo colors red and blue represent docking strands P₁ and P₂, respectively.

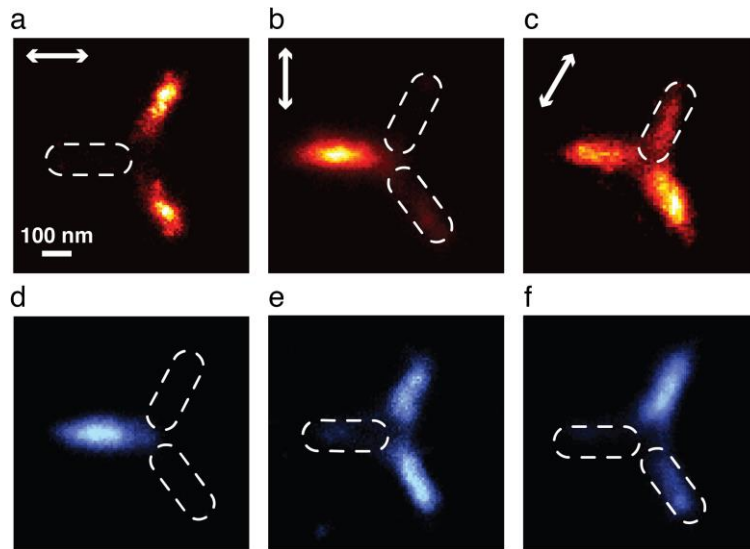


Figure S6. Controlling thiol-desorption and ligand replacement from gold nanotrimer structures with polarized light illumination. Average super-resolved metallic DNA-PAINT images of n individual gold nanotrimers carrying two DNA docking strand species (pseudo colors red and blue for docking strands P_1 and P_2 , respectively). The dual functionalization of the nanostructures was achieved by first, irradiating the antenna with a linearly polarized femtosecond pulsed laser (950 nm, 1.7 mJ/cm^2) at 0° (**a** and **d**), 90° (**b** and **e**) or 120° (**c** and **f**) and then, by re-functionalization with the thiol-reactive docking strand P_2 . Imaging of individual targets using the same fluorophore was performed by a round of acquisition with imager strand P_1^* , followed by a washing step, and the sequential incubation of imager strand P_2^* . m-PAINT movies were acquired using a 1 or 2 nM concentration of imager strand P_1^* (**a**, **b**, **c**) or P_2^* (**d**, **e**, **f**) in imaging buffer C, respectively. n and the mean number of localizations in individual images is 28 and 776 ± 480 , 34 and $1,348 \pm 545$, 34 and $1,946 \pm 552$, 28 and $1,080 \pm 597$, 34 and $1,426 \pm 721$, 34 and $2,338 \pm 1,019$ for **a**, **b**, **c**, **d**, **e**, **f**, respectively.

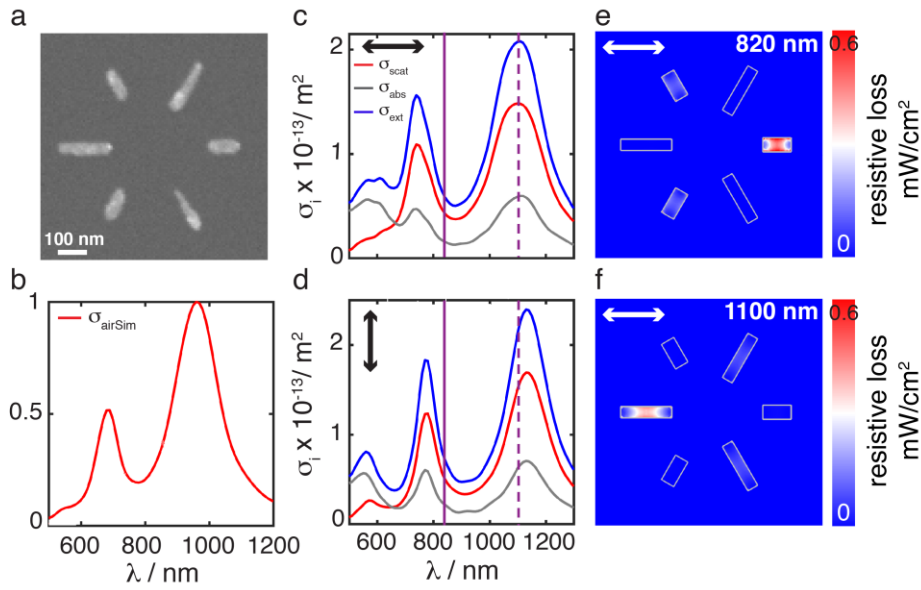


Figure S7. Plasmonic response of six-leg gold nanostructures. **a**, SEM image of a six-leg gold nanostructure composed of two sizes of nanorods with dimensions of $110 \times 45 \text{ nm}^2$ and $180 \times 40 \text{ nm}^2$. **b**, FDTD-simulated single-antenna scattering spectra in air. **c**, **d**, Simulated scattering (red), absorption (grey) and extinction (blue) spectra in water for parallel and perpendicular polarized illumination, respectively. Violet lines highlight the laser wavelength used in the desorption experiments (820 or 1100 nm). **e**, **f**, Comsol simulations of the resistive loss distribution at 820 nm or at 1100 nm after femtosecond laser irradiation of 1.9 mJ/cm^2 or 3.8 mJ/cm^2 in water for parallel incident polarization, respectively. Color scale bars represent the resistive losses values in mW/nm^3 .

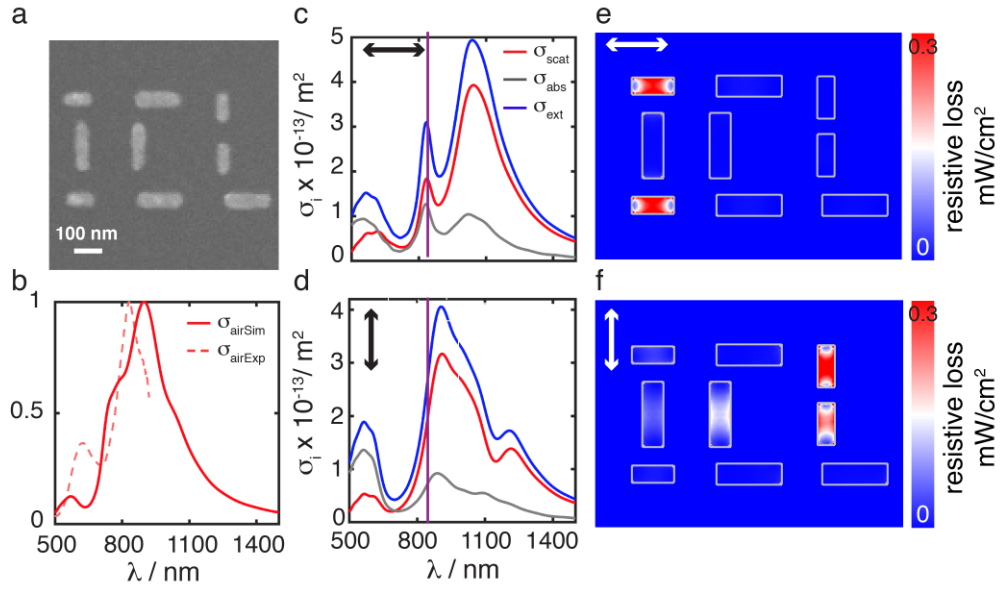


Figure S8. Plasmonic response of ‘ICL’ gold nanostructures. **a**, SEM image of a gold custom-design letter pattern (‘ICL’) nanostructure composed of two sizes of nanorods with dimensions of $110 \times 45 \text{ nm}^2$ and $170 \times 50 \text{ nm}^2$. **b**, FDTD-simulated (full line) and measured (dashed line) single-antenna scattering spectra in air. **c**, **d**, Simulated scattering (red), absorption (grey) and extinction (blue) spectra in water for parallel and perpendicular polarized illumination, respectively. Violet lines highlight the laser wavelength used in the desorption experiments (820 nm). **e**, **f**, Comsol simulations of the resistive loss distribution at 820 nm after femtosecond laser irradiation of 2.6 mJ/cm^2 in water for parallel and perpendicular incident polarization, respectively. Color scale bars represent the resistive losses values in mW/nm^3 .

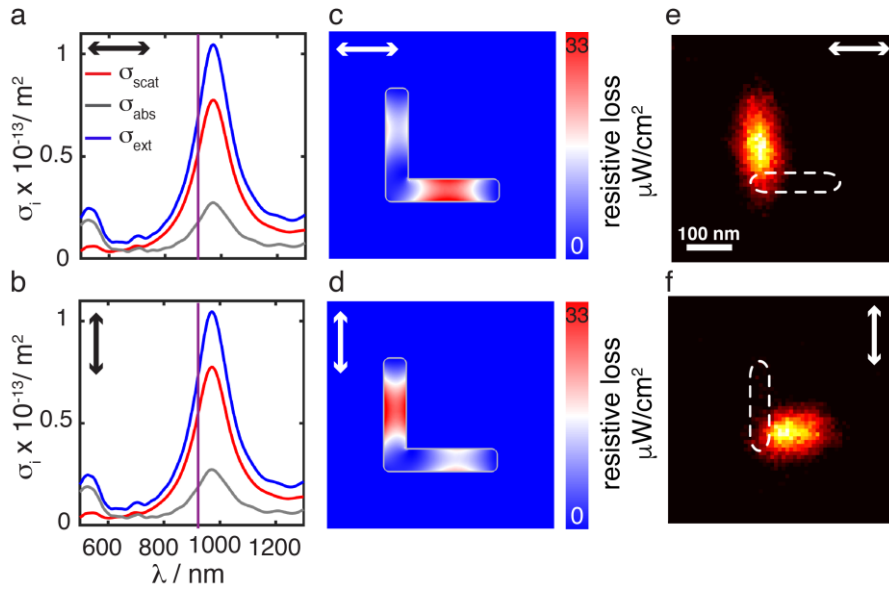


Figure S9. Plasmonic response of ‘L’ gold nanostructures. **a, b,** Simulated scattering (red), absorption (grey) and extinction (blue) spectra of a L-shape gold nanostructure composed of two connected nanorods, with dimensions of $200 \times 40 \text{ nm}^2$, in water for parallel and perpendicular polarized illumination, respectively. Violet line highlights the laser wavelength used in the desorption experiments (950 nm). **c, d,** Comsol simulations of the resistive loss distribution at 950 nm after femtosecond laser irradiation of 5.3 mJ/cm^2 in water for parallel and perpendicular incident polarization, respectively. Color scale bars represent the resistive losses values in $\mu\text{W}/\text{cm}^2$. **g, h,** Average super-resolved metallic DNA-PAINT images of n individual gold nanostructures functionalized with docking strand P_1 after irradiation with a 950 nm linearly polarized femtosecond pulsed laser of 5.3 mJ/cm^2 fluence. White arrows represent the polarization of the incident light. m-PAINT movies were collected using 5 nM of imager strand P_1^* . n and the mean number of localizations in individual images are 33 and 701 ± 436 , 30 and 634 ± 448 , respectively.

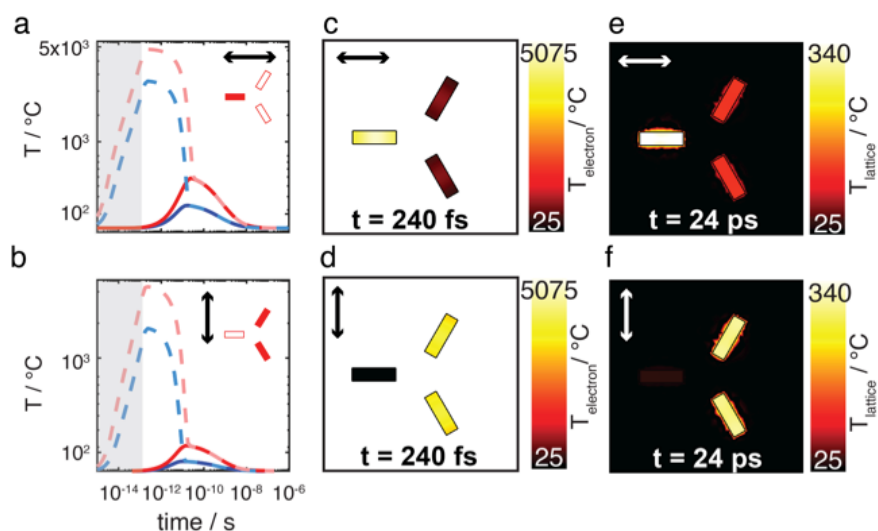


Figure S10. Numerical calculation of temperature profiles of plasmon-selective Au-S desorption on gold nanotrimers. **a, b**, Simulated temporal evolution of the electron temperature (dashed line) and lattice temperature (full line) for the horizontal and vertical elements of a gold nanotrimer structure composed of three identical nanorods with dimension of $180 \times 55 \text{ nm}^2$ following femtosecond laser irradiation (0° , 950 nm) at 0.6 mJ/cm^2 (blue) and 2.0 mJ/cm^2 (red) fluence. **c-f**, Map distribution of the electron temperature (**c, d**) and the lattice temperature (**e, f**) following femtosecond laser irradiation at 240 fs and 24 ps delayed after the temporal start of a 180 fs laser pulse. Black and white arrows represent the polarization of the incident light.

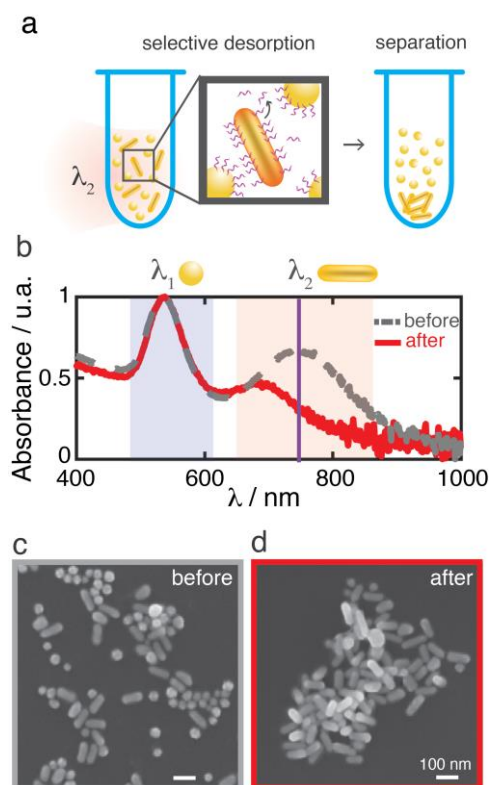


Figure S11. Solution-based sorting of metal nanoparticles. **a**, Au nanoparticles and nanorods modified with a self-assembly monolayer of 6-mercapto-1-hexanol are illuminated with a linearly polarized femtosecond laser at the nanorod local surface plasmon resonance wavelength (750 nm, 8 mJ/cm²). S-Au desorption from Au nanorods induces the aggregation of the nanorods in the solution. **b**, Absorbance spectra and **c**, **d**, representative SEM images of the 50 nm Au nanoparticles and the 50×150 nm² Au nanorods solution mixture before (**c**) and after (**d**) laser irradiation.

Supporting References

- (S1) Pensa, E.; Cortés, E.; Corthey, G.; Carro, P.; Vericat, C.; Fonticelli, M. H.; Benítez, G.; Rubert, A. A.; Salvarezza, R. C. The Chemistry of the Sulfur-Gold Interface: In Search of a Unified Model. *Acc. Chem. Res.* **2012**, *45*, 1183–1192.
- (S2) Herne, T. M.; Tarlov, M. J. Characterization of DNA Probes Immobilized on Gold Surfaces. *J. Am. Chem. Soc.* **1997**, *119*, 8916–8920.
- (S3) Hohlfeld, J.; Wellershoff, S.-S.; Güdde, J.; Conrad, U.; Jähnke, V.; Matthias, E. Electron and Lattice Dynamics Following Optical Excitation of Metals. *Chem. Phys.* **2000**, *251*, 237–258.
- (S4) Paddock, C. A.; Eesley, G. L. Transient Thermoreflectance from Thin Metal Films. *J. Appl. Phys.* **1986**, *60*, 285–290.
- (S5) Elsayed-Ali, H. E.; Norris, T. B.; Pessot, M. A.; Mourou, G. A. Time-Resolved Observation of Electron-Phonon Relaxation in Copper. *Phys. Rev. Lett.* **1987**, *58*, 1212–1215.
- (S6) Anisimov, S. I.; Kapeliovich, B. L.; Perel-man, T. L. Electron Emission from Metal Surfaces Exposed to Ultrashort Laser Pulses. *J. Exp. Theor. Phys.* **1974**, *66*, 375–377.
- (S7) Chen, J. K.; Beraun, J. E. Numerical Study of Ultrashort Laser Pulse Interactions With Metal Films. *Numer. Heat Transf. Part A Appl.* **2001**, *40*, 1–20.
- (S8) Ashcroft, N. W.; Mermin, N. D. Solid State Physics. *Solid State Physics*, 1976, *2*, 848.
- (S9) Lin, Z.; Zhigilei, L. V.; Celli, V. Electron-Phonon Coupling and Electron Heat Capacity of Metals under Conditions of Strong Electron-Phonon Nonequilibrium. *Phys. Rev. B - Condens. Matter Mater. Phys.* **2008**, *77*, 75133.
- (S10) Boulais, É.; Lachaine, R.; Meunier, M. Plasma Mediated off-Resonance Plasmonic Enhanced Ultrafast Laser-Induced Nanocavitation. *Nano Lett.* **2012**, *12*, 4763–4769.
- (S11) Ho, C. Y.; Powell, R. W.; Liley, P. E. Thermal Conductivity of the Elements: A Comprehensive Review. *J. Phys. Chem. Ref. Data* **1974**, *3*, 1–796.
- (S12) Zijlstra, P.; Chon, J. W. M.; Gu, M. White Light Scattering Spectroscopy and Electron Microscopy of Laser Induced Melting in Single Gold Nanorods. *Phys. Chem. Chem. Phys.* **2009**, *11*, 5915–5921.